www.acsnano.org

Tailoring the Electron—Phonon Interaction in Au₂₅(SR)₁₈ Nanoclusters via Ligand Engineering and Insight into Luminescence

Zhongyu Liu, Yingwei Li, Ellen Kahng, Shan Xue, Xiangsha Du, Site Li, and Rongchao Jin*



Downloaded via CARNEGIE MELLON UNIV on August 6, 2023 at 15:14:44 (UTC). See https://pubs.acs.org/sharingguidelines for options on how to legitimately share published articles.

Cite This: ACS Nano 2022, 16, 18448-18458



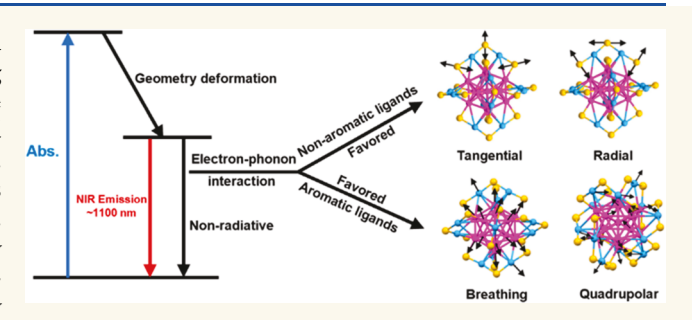
ACCESS

Metrics & More

Article Recommendations

s Supporting Information

ABSTRACT: Understanding the electron–phonon interaction in Au nanoclusters (NCs) is essential for enhancing and tuning their photoluminescence (PL) properties. Among all the methods, ligand engineering is the most straightforward and facile one to design Au NCs with the desired PL properties. However, a systematic understanding of the ligand effects toward electron–phonon interactions in Au NCs is still missing. Herein, we synthesized four $\operatorname{Au}_{25}(\operatorname{SR})_{18}^-$ NCs protected by different –SR ligands and carefully examined their temperature-dependent band-gap renormalization behavior. Data analysis by a Bose–Einstein two-oscillator model revealed a suppression of



high-frequency optical phonons in aromatic-ligand-protected Au_{25} NCs. Meanwhile, a low-frequency breathing mode and a quadrupolar mode are attributed as the main contributors to the phonon-assisted nonradiative relaxation pathway in aromatic-ligand-protected Au_{25} NCs, which is in contrast with non-aromatic-ligand-protected Au_{25} NCs, in which tangential and radial modes play the key roles. The PL measurements of the four Au_{25} NCs showed that the suppression of optical phonons led to higher quantum yields in aromatic-ligand-protected Au_{25} NCs. Cryogenic PL measurements provide insights into the nonradiative energy relaxation, which should be further investigated for a full understanding of the PL mechanism in Au_{25} NCs.

KEYWORDS: atomically precise nanoclusters, Au₂₅, electron-phonon coupling, two-oscillator model, photoluminescence, ligand effect

INTRODUCTION

Atomically precise Au nanoclusters (NCs) exhibit rich optical and optoelectronic properties and have recently attracted considerable research interest for diverse applications in solar cells, photocatalysis, bioimaging, sensing, etc.^{1–6} Particularly, Au NCs are found to present good biocompatibility and intriguing near-infrared photoluminescence (NIR-PL) that are rare in classical materials (e.g., organic dyes).^{7–10} The NIR-PL quantum efficiency and emission wavelength can be altered by varying the core structure (with the same ligands) or the protecting ligands (with the same core structure). 11,12 Compared to the design and synthesis of different structured Au NCs, ligand engineering is an easier way to tune the PL properties and exploit the full potential of known Au NCs. 13-15 When different protecting ligands are introduced into the cluster system, the local electron density and vibrational properties of Au NCs can be changed, which alters the energy relaxation pathway via electron-phonon interactions. 16 However, the nature of electron-phonon interactions in Au NCs still lacks an understanding, and the attainment of such information will

provide guidance toward tailoring Au NCs with the desired photoluminescence properties.

Fundamental studies on the electron—phonon interactions can be carried out by cryogenic optical absorption spectroscopy. This technique has made it possible to measure the temperature-dependent band-gap renormalization and extract vibrational relaxation pathways that couple with the corresponding electronic transition. Of note, vibrational relaxation is the main nonradiative energy relaxation pathway; hence, a comprehensive understanding of electron—phonon interaction in Au NCs is of paramount importance for improving their luminescence properties. The development of cryogenic optical absorption measurements is built on a generally accepted

Received: July 4, 2022 Accepted: October 7, 2022 Published: October 17, 2022





ACS Nano www.acsnano.org Article

theory that the temperature dependence of a band gap $(E_{\rm g})$ is a joint contribution from both lattice thermal expansion and electron—phonon interaction. Generally, under the quasi-harmonic approximation, the contribution of the two mechanisms can be written as

$$\frac{\mathrm{d}E_{\mathrm{g}}}{\mathrm{d}T} = \left(\frac{\partial E_{\mathrm{g}}}{\partial T}\right)_{\mathrm{TE}} + \sum_{j,\vec{q}} \frac{\partial E_{\mathrm{g}}}{\partial n_{j,\vec{q}}} \left(n_{j,\vec{q}} + \frac{1}{2}\right) \tag{1}$$

where the first term represents the contribution from the lattice thermal expansion (TE) and the second term describes the contribution of electron—phonon interaction from all the phonon branches in the system. However, the above formula cannot be directly applied to analyze the measured temperature-dependent $E_{\rm g}$ data because the second term is extremely complicated to obtain in first-principles simulations. Thus, important approximations have been made to build parametric models that bridge the gap between theoretical analysis and experimental data.

To solve the problem, a Bose–Einstein oscillator model was established, and it successfully extracted electron–phonon interaction information for various semiconductor materials. 22,23 The formula of the Bose–Einstein oscillator model is given in eq 2, where $E_g(0)$ represents the band gap at 0 K, $\hbar\omega$ denotes the energy of phonon modes that contribute to the renormalization of the band gap, and α is a constant. Of note, W_i is a normalization constant. The success of the Bose–Einstein oscillator model is that it adopts an approximation where the contribution of thermal expansion can be rewritten to a formula similar to that of the electron–phonon interaction term. In other words, both types of mechanisms have been shown to vary with temperature just as phonon occupation number which follows the Bose–Einstein distribution.

$$E_{g}(T) = E_{g}(0) - \alpha \sum_{i=1}^{N} W_{i} \frac{\hbar \omega}{\exp\left(\frac{\hbar \omega}{k_{B}T}\right) - 1}$$
(2)

s. t.
$$\sum_{i=1}^{N} W_i = 1$$

In the field of Au NCs, Ramakrishna et al. used the O'Donnell-Chen model, which is a variant of the Bose-Einstein single-oscillator model, to describe the temperaturedependent (room temperature down to 78 K) band gap of Au₂₅ and Au₃₈ NCs.¹⁷ Later works showed that such a model is also effective for other Au NCs and can be extended to a wider temperature range (rt down to 4 K). ^{18,24} As shown in eq 3, the O'Donnell-Chen model takes only one oscillator to approximate the contribution from all phonon modes. Although this single-oscillator model is found to fit the experimentally obtained temperature-dependent band gap quite well, the physical meaning of the hypothesized single oscillator can be ambiguous in some cases. Actually, in a sophisticated system such as Au₂₅ NCs, both low-frequency acoustic phonons and high-frequency optical phonons exist and affect the electronic transition from the highest occupied molecular orbital (HOMO) to the lowest unoccupied molecular orbital (LUMO). 25,26 Thus, both phonon types should be taken into consideration in order to obtain an adequate picture of these NCs.

$$\begin{split} E_{\rm g}(T) &= \\ &= \underbrace{E_{\rm g}(0) - \alpha\hbar\omega/[\exp(\frac{\hbar\omega}{k_{\rm B}T}) - 1]}_{\text{Bose-Einstein single oscillator}} &= E_{\rm g}(0) - \alpha\hbar\omega[\coth(\frac{\hbar\omega}{2k_{\rm B}T}) - 1] \\ &= O\text{'Donnell-Chen} \end{split}$$

In the current work, we perform temperature-dependent (down to liquid helium temperature) absorption spectroscopic analyses on four $\mathrm{Au}_{25}(\mathrm{SR})_{18}^-$ NCs protected by different – SR ligands (R = C₆H₅–CH₂CH₂–, C₆H₅–CH₂–, C₆H₅–, 3,5-DiMe-C₆H₃–) in order to understand the ligand effect on the vibrational energy relaxation pathway. A Bose–Einstein two-oscillator model is introduced to separate the contributions from acoustic phonons and optical phonons toward the band-gap renormalization in Au_{25} NCs. Our analysis shows that, compared to nonaromatic ligands, the aromatic ligands are able to suppress high-frequency optical phonons in Au_{25} NCs and promote radiative relaxation of photoexcited electrons.

RESULTS AND DISCUSSION

The syntheses of Au₂₅ NCs protected by 2-phenylethylenethiol (denoted as PET) and benzyl mercaptan (BM), respectively, follow a previously reported one-pot procedure. 27,28 In addition, two aromatic ligands (thiophenol and 3,5-dimethylbenzenethiol, denoted as HSPh and 3,5-DMBT, respectively) are also used to protect Au₂₅ NCs and their syntheses are via a ligandexchange-induced structure transform (LEIST) methodology that starts with Au₂₃(SR)₁₆^{-.29} The structures of the four thiols are given in the inset of Figure 1. The room-temperature UV-vis spectra of the four Au₂₅ NCs are measured and compared in Figure 1. The characteristic peak of $Au_{25}(PET)_{18}^{-}$ at around 675 nm is red-shifted to 688, 695, and 700 nm for $Au_{25}(BM)_{18}^{-}$, $Au_{25}(SPh)_{18}^-$, and $Au_{25}(3.5-DMBT)_{18}^-$, respectively, which is caused by the stronger electron delocalization and is consistent with a previous report.³⁰ Of note, DFT simulations identified that the absorption peak discussed above is from the HOMO-1

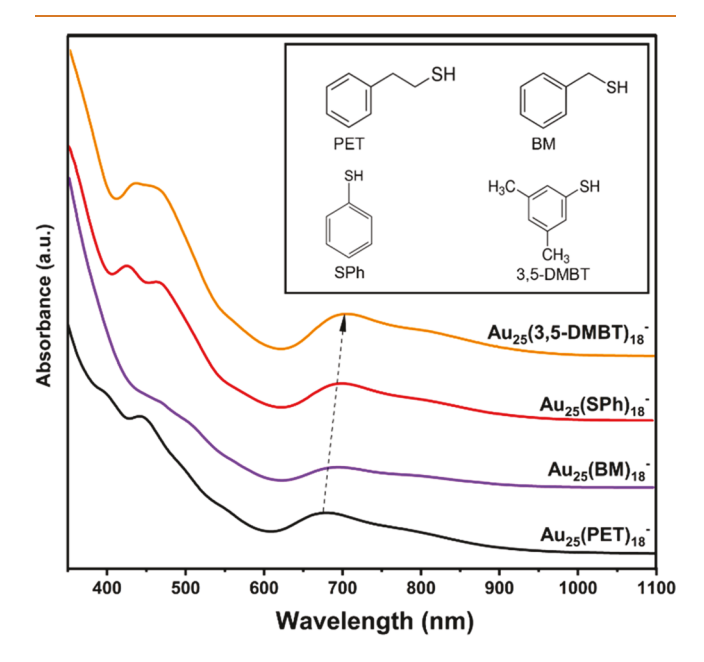


Figure 1. Room-temperature UV–vis absorption spectra of four $\mathrm{Au}_{25}(\mathrm{SR})_{18}^-$ (counterion: ${}^{\dagger}\mathrm{N}(\mathrm{C}_8\mathrm{H}_{17})_4$) NCs protected by different ligands (inset: molecular structures of the four thiols used).

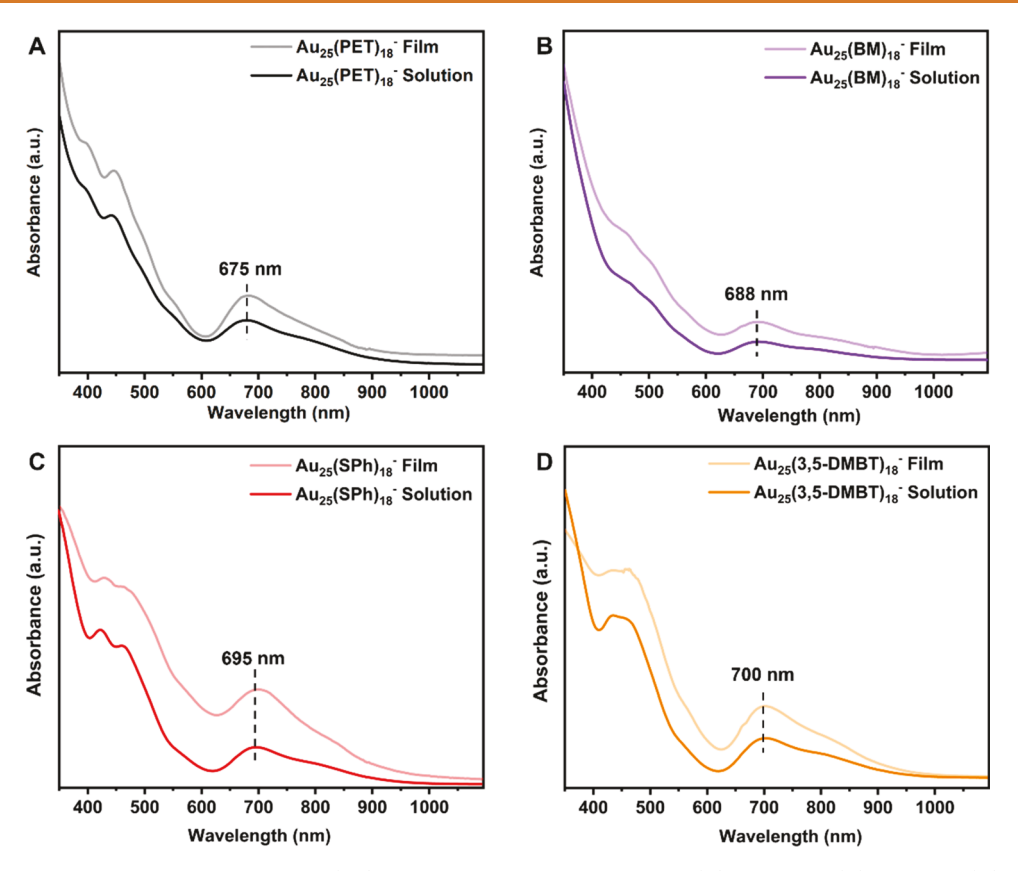


Figure 2. Room-temperature UV-vis spectra of $Au_{25}(SR)_{18}^-$ NCs in solution and thin film: (A) SR = PET, (B) SR = BM, (C) SR = SPh, and (D) SR = 3.5-DMBT.

to LUMO transition.³¹ The less prominent shoulder band at \sim 800 nm originates from the HOMO–LUMO transition and follows the same ligand-dependent red-shift trend as does the HOMO-1 to LUMO transition. A peak deconvolution protocol is applied below to decouple these two peaks and extract the accurate value of the HOMO–LUMO gap ($E_{\rm g}$). An analysis of the absorption coefficients for the four Au₂₅ NCs is given in Figure S1, where all four samples have similar values in the 600–900 nm region, suggesting that the different ligands barely affect the core electronic states.

To carry out the cryogenic optical absorption measurements, each of the four ${\rm Au}_{25}$ NCs is uniformly embedded in polystyrene thin films via a drop-cast method. To evaluate the quality of asobtained thin films, the room-temperature UV—vis absorption spectra of four ${\rm Au}_{25}$ NCs are measured in both film and solution states. As shown in Figure 2A—D, the absorption profiles of the thin-film spectra are consistent with their solution counterparts, despite a slight broadening and trivial shift. Such broadening and shift is commonly observed and can be ascribed to a stronger coupling between electronic states and vibrational states in the solid state. 32,33 Hence, the thin films are of good quality and can be employed to understand the electronic and optical properties of ${\rm Au}_{15}$ NCs.

The temperature-dependent optical absorption measurements are conducted from rt down to liquid helium (LH) temperature to understand the ligand effect on the electron—phonon interaction in Au_{25} NCs. The obtained temperature-dependent optical absorption spectra are then transformed to the photon energy scale (Figure 3A—D, left) for further analysis. The transformation is done by substituting the ordinary y axis with $A \cdot \lambda^2$ (where A is the absorbance and λ is the wavelength in

nm) and the x axis with photon energy (i.e., $1241/\lambda$). To extract accurate peak positions, two Gaussian profiles are used to deconvolute the absorption profile between 1.3 and 2.1 eV at each temperature (Figure 3A–D, upper right). The absorption maximum of the Gaussian peak at around 1.6 eV is the value of $E_{\rm g}$. The

The temperature-dependent spectra show that, for all four samples, the absorption peaks become narrower and sharper as the temperature decreases, suggesting a decoupling of electronic states and vibrational states. 17 The decoupling occurs because the phonon population follows the Bose-Einstein distribution and approaches zero as the temperature goes to zero. Interestingly, the E_{σ} values of the four Au₂₅ NCs protected by different ligands all show a monotonous blue shift as the temperature drops (Figure 3A-D, bottom right), which is similar to conventional semiconductors such as Si, GaAs, etc.²¹ Of note, the observed monotonous blue-shift trend with a decrease in temperature is not guaranteed for all semiconductor materials; indeed, a monotonous red-shift trend and even a zigzag pattern have been observed in perovskite materials. 19,34 Therefore, a well-rounded analysis of temperature-dependent E_{σ} is essential to understand the key factors that cause such differences across various types of materials.

In contrast to previous work where only one Bose–Einstein oscillator was employed to describe the temperature-dependent trend of $E_{\rm g}^{17,18}$ here we introduce a Bose–Einstein two-oscillator formula (eq 4) to model the observed temperature-dependent trend and separate contributions from optical phonons and acoustic phonons. In eq 4, $E_{\rm g}(0)$ represents the gap at 0 K, $k_{\rm B}$ is the Boltzmann constant, T is the temperature in kelvin, α is a constant, and $\hbar\omega_{\rm OP}$ and $\hbar\omega_{\rm AP}$ are the average

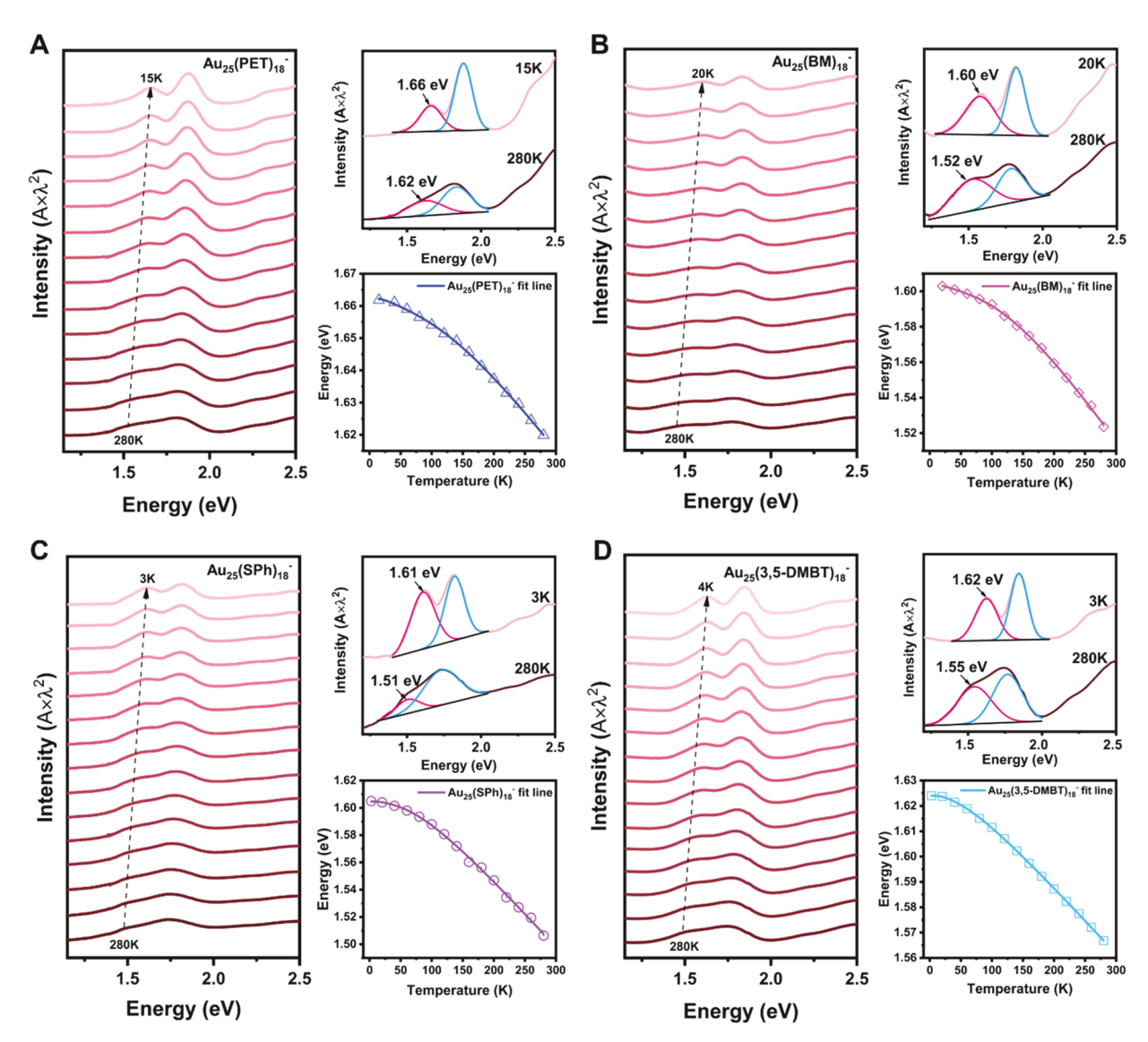


Figure 3. (A–D, left panels) Temperature-dependent absorption spectra of four $\mathrm{Au}_{25}(\mathrm{SR})_{18}^-$ NCs (photon energy scale). (A–D, top right panels) Peak deconvolution of spectra at 280 K and cryogenic temperatures. (A–D, bottom right panels) Extracted E_{g} values and fittings by the Bose–Einstein two-oscillator model.

energies for optical phonons and acoustic phonons, respectively, with W_1 and W_2 being their corresponding normalization constants.

$$E_{g}(T) = E_{g}(0) - \alpha \left(W_{1} \frac{\hbar \omega_{OP}}{\exp\left(\frac{\hbar \omega_{OP}}{k_{B}T}\right) - 1} + W_{2} \frac{\hbar \omega_{AP}}{\exp\left(\frac{\hbar \omega_{AP}}{k_{B}T}\right) - 1} \right)$$

$$s. t. W_{1} + W_{2} = 1$$
(4)

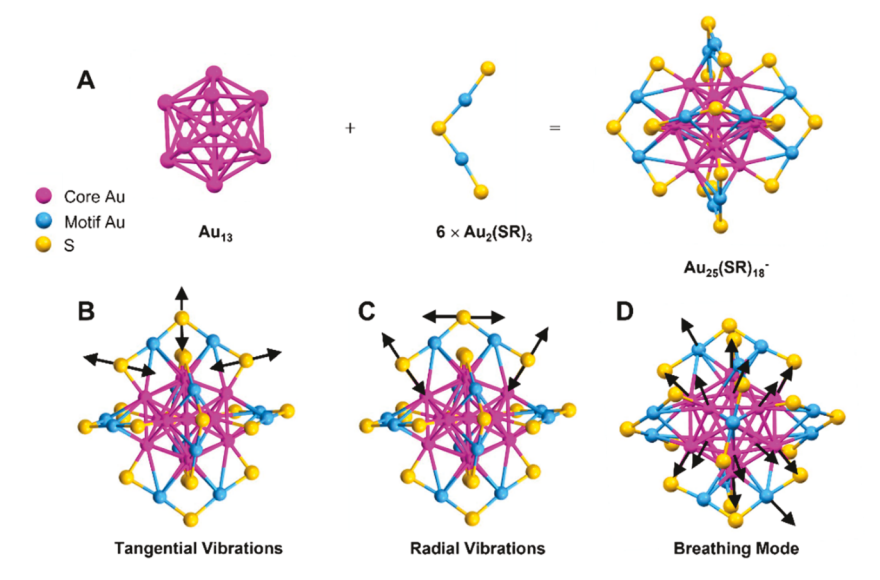
The introduction of a Bose—Einstein two-oscillator model here depends on two basic approximations. The first is the effect from lattice thermal expansion incorporated into these two terms, and its contribution is trivial compared to electron—phonon interactions. As illustrated in eq 2, if one wants to model the accurate thermal expansion contribution, at least one more

Bose—Einstein term should be included, which significantly increases the number of parameters that need to be optimized and might lead to serious underfitting problems. An alternative way to calculate the thermal expansion contribution is to rewrite the thermal expansion term (see eq 5), where α is the thermal expansion coefficient, B is the bulk modulus, and $\frac{\partial E_g}{\partial P}$ is the pressure coefficient of E_g . ^{19,21}

$$\frac{\partial E_{g}}{\partial T} = \frac{\partial E_{g}}{\partial V} \frac{\partial V}{\partial T} = -\frac{\partial E_{g}}{\partial P} \left| \frac{\partial P}{\partial V} \right| \frac{\partial V}{\partial T} = -\alpha \cdot B \cdot \frac{\partial E_{g}}{\partial P}$$
(5)

An approximate calculation of eq 5 can be rationalized as follows. First, previous temperature-dependent X-ray absorption fine structure studies of Au₂₅ NCs showed that the average length of Au–Au bonds shrinks by less than 1% when the temperature decreases from 298 to 90 K.³⁸ From the definition of the thermal expansion coefficient, α can thus be estimated as 1 × 10⁻⁴ K⁻¹. The modulus of Au NCs has never been experimentally measured, but a previous study of nanomaterials below a 10 nm scale showed that the modulus of nanomaterials

Scheme 1. (A) X-ray Structure of Au₂₅ NCs (Core, Surface Staple-Like Motifs, and the Total Structure), (B) Tangential Vibrations of the Au₂(SR)₃ Motifs, (C) Radial Vibrations of Au₂(SR)₃ Motifs, and (D) Breathing Mode of the Au₁₃ Core^a



^aRedrawn from refs 25 and 46. The C and H atoms are omitted for clarity.

can be slightly larger than that of their bulk counterpart.³⁹ Hence, a reasonable value of B is between 2×10^2 and 8×10^2 GPa. Of note, the modulus of bulk Au is 180 GPa. A rough value of the pressure coefficient of E_{φ} can be approximated from the high-pressure photoluminescence and absorption experiments by Li et al. 40,41 Different Au NCs showed different pressuredependent trends of E_g , but the absolute value of $\frac{\partial E_g}{\partial P}$ is around $10^{-3}\ eV/GPa$ in magnitude. Taken together, the thermal expansion effect can be approximated to be between 10⁻⁴ and 10^{-5} eV/K. Hence, when the temperature decreases from rt to 3 K, the thermal expansion will account for a shift of between 0.03 and 0.003 eV. The upper bound (0.03 eV) of our estimation is close to the observed overall temperature-induced $E_{\rm g}$ shift of Au₂₅ NCs (0.04-0.1 eV). A possible overestimation here is the measurement of $\frac{\partial E_g}{\partial P}$ performed at rt, 40,41 which inevitably incorporates significant contributions from electron-phonon interactions. The pressure-induced changes in lattice parameters not only modify the electronic transition but also affect the harmonic frequencies of the lattice.⁴² Thus, extra physical measurements are required to obtain a more accurate evaluation of the thermal expansion effect. Meanwhile, previous work on a variety of semiconductors revealed that the thermal expansion effect is commonly overwhelmed by electron-phonon interactions. 22,43 Summarizing all the above factors and considerations, the contribution of the thermal expansion mechanism is not dominant, and incorporating this effect will not cause significant errors in our data analysis.

The second assumption here is that both electron-optical-phonon scattering and electron-acoustic-phonon scattering should be considered for a better understanding of the role of the ligand in the energy relaxation process. Generally, three main electron—phonon scattering mechanisms are accepted: deformation potential scattering, Fröhlich scattering, and piezo-electric scattering. He Piezoelectric scattering is not expected in Au₂₅ NCs because a noncentrosymmetric packing pattern is necessary for materials to possess piezoelectricity, but previous single-crystal X-ray diffraction measurements revealed that Au₂₅

NCs possess a centrosymmetric icosahedral core (Scheme 1A).²⁷ Fröhlich scattering is the Coulomb interaction between the electrons and the electric field induced by out-of-phase displacements of atoms with opposite charges (optical phonons). For example, in the case of Au₂₅ NCs, the radial and tangential Au-S vibrations (Scheme 1B,C) of the SR-Au-SR-Au-SR motif can couple with the HOMO-to-LUMO electronic transition via a Fröhlich interaction. 45,46 Early works by Ramakrishna et al. studied the temperature dependence (down to 77 K) of the E_g values of Au_{25} NCs and found that the optical phonons contribute significantly to the band-gap shift in this temperature regime. 17,24 However, only considering the effects from optical phonons is not enough in our experiments (down to ~4 K). On one hand, our previous work found a suppression of motif phonons in $Au_{25}(PET)_{18}^{-1}$ thin films. ¹⁸ On the other hand, optical phonons typically have energies of tens of meV, which means that their population will be extremely small at low temperatures (<100 K). Hence, acoustic phonons should play a prominent role in affecting the $E_{\rm g}$ shift over this regime and thus need to be carefully studied. Commonly, the electronacoustic-phonon scattering is achieved via deformation potential scattering. The deformation potential is a linear coefficient used to describe the effects of lattice distortion toward singleelectron-band energy. In spherical nanostructures, the breathing mode is acknowledged to be the fundamental acoustic vibration mode and it has been found to be of paramount importance for deformation scattering in quantum dots. 47,48 So far, the breathing mode of Au₂₅ NCs (Scheme 1D) has been studied by a variety of methods, including Raman spectroscopy, transient absorption spectroscopy (TAS), and density functional theory simulations (DFT). 25,49,50 However, its effect on E_{σ} renormalization remains unknown and needs more work. It is worth noting that optical phonons can also interact with electrons through nonpolar deformation potentials at higher temperatures. 51-53 Nevertheless, such an interaction is trivial compared to the Fröhlich interaction and can thus be neglected.

Our discussions above have demonstrated that the Bose–Einstein two-oscillator model is suitable for modeling the electron–phonon interactions in Au₂₅ NCs, albeit it incorpo-

rates slight effects from thermal expansion. As shown in Figure 3A–D, bottom right, the Bose–Einstein two-oscillator model showed a good fitting to our measured data. The extracted electron–phonon information is given in Table 1. It is interesting to find that the acoustic phonon modes coupled with the electronic transitions are similar among the four Au₂₅ NCs, while the coupled optical phonon mode changes drastically from aromatic-ligand-protected Au₂₅ NCs to non-aromatic-ligand-protected ones. A careful assignment of these phonon modes is required before we can generate a full picture of the energy relaxation process in Au₂₅ NCs. Therefore, we compare the average phonon energy obtained from our model with the previously reported TAS, ^{25,54–56} Raman spectroscopy, ^{46,50} and DFT simulations ^{25,49} to identify the main contributors in the modeled oscillators.

As shown in Table 1, the average frequency of the acoustic phonon mode that couples with the HOMO-to-LUMO transition is determined to be around 60 cm⁻¹ (7.6 meV \times 8.0 $cm^{-1}/meV = 60$) in PET-protected Au₂₅ and around 40 cm⁻¹ in all other Au₂₅ NCs. Interestingly, the modeled acoustic phonon modes here have energies similar to those of the Au₂₅ core breathing mode and quadrupolar-like mode (Figure S2) that were determined in previous femtosecond pump-probe measurements and DFT simulations. 25 In detail, the breathing mode and quadrupolar-like mode in Au₂₅(PET)₁₈⁻ are induced by the amplitude and frequency modulation of the HOMO-to-LUMO electronic transition, respectively.^{54–56} In the case of $Au_{25}(PET)_{18}^{-}$, the frequency of the quadrupolar-like mode is determined to be around 40 cm⁻¹ and the frequency of the breathing mode is around 80 cm⁻¹. 25,54,55 Therefore, our modeled acoustic oscillator (60 cm⁻¹) in Au₂₅(PET)₁₈⁻ can be considered as taking contributions from both the breathing mode and the quadrupolar-like mode. Moreover, Kong et al. recently found that these acoustic phonon modes are invariant in Au₂₅ NCs protected by different ligands, including both aromatic and nonaromatic ligands. 54 Hence, the electronacoustic-phonon interactions in all three other Au_{25} NCs should be similar to the case of $Au_{25}(PET)_{18}^{-}$. The relatively smaller average energy of fitted acoustic oscillators indicates a greater involvement of the low-frequency quadrupolar-like mode. Furthermore, as illustrated in Scheme 1D, the breathing mode is the in-phase radially symmetric oscillations of all Au atoms in the Au₁₃ core, which approximately have a linear effect on the single-electron-band energy.⁴⁷ Meanwhile, the quadrupolar-like mode, where periodic expansions and contractions happen along one direction while synchronous out-of-phase oscillations happen in the perpendicular plane, leads to an atomic displacement similar to that of static strain.⁵⁷ Overall, both acoustic vibration modes should interact with the HOMO-to-LUMO electronic transition via deformation potential scatter-

Table 1. Fitted Parameters for the Four Au₂₅ NCs

ligand	$E_{\rm g}(0)$	$\alpha (10^{-4})$	W_1	$\hbar\omega_{ m OP} \ ({ m meV})$	W_2	$\hbar\omega_{ m AP} \ ({ m meV})$
SCH ₂ CH ₂ Ph (PET)	1.66	2.8	0.58	48.0	0.42	7.6
SCH ₂ Ph (BM)	1.60	5.5	0.75	41.1	0.25	5.1
SPh	1.61	5.1	0.71	24.5	0.29	5.0
$SPh(CH_3)_2$ (3,5-DMBT)	1.62	2.7	0.55	20.6	0.45	4.6

We next discuss the optical phonons (Table 1). In a complicated system such as Au₂₅ NCs, the number of optical phonon branches is much greater than that of acoustic phonon branches, which leads to a great difficulty in assigning optical phonon modes. To simplify the problem, we neglect the effect of C=C, C-C, and C-H vibrations from the carbon tail and treat the carbon tail as a whole when we discuss their effect. It is reasonable because the vibrations of light atoms (i.e., C, H) are far beyond the frequency region that we are interested in. 58 Therefore, the possible origin of optical phonons can be narrowed down to the Au(inner core)-(SR)-Au(motif)-(SR)-Au(motif)-(SR)-Au(inner core) chain. The observed 330 cm⁻¹ optical phonon mode in $Au_{25}(BM)_{18}^{-}$ and 390 cm⁻¹ optical phonon mode in Au₂₅(PET)₁₈ are close to the Au–S vibration modes in the Au₂(SR)₃ motifs measured by Raman spectroscopy. 46,50 Specifically, the frequency of radial and tangential Au-S vibrations in Au₂(PET)₃ have been determined to be between 300 and 330 cm⁻¹. Moreover, the nature of these two vibrational modes can induce a changing electromagnetic field that can interact with the free electron via a Fröhlich interaction. Hence, we believe that these two phonon modes are the main contributors to the modeled optical oscillators in $Au_{25}(PET)_{18}^{-}$ and $Au_{25}(BM)_{18}^{-}$.

In the case of aromatic-ligand-protected $Au_{25}(SPh)_{18}^{-}$ and $Au_{25}(3.5-DMBT)_{18}^{-}$, the energies of the observed optical phonon oscillators are around 200 and 170 cm⁻¹, respectively, which are much lower than those of non-aromatic-ligandprotected NCs. The length of the carbon tail had been found to affect the Au-S vibrational frequency because the frequency of harmonic oscillators is mass-related. 60 However, the difference between SPh and BM is just one -CH₂ group and 3,5-DMBT actually shares the same molecular weight with PET. Therefore, the Au-S vibration in the motif should not vary much and the observed changes actually suggest that the aromatic ligands suppress the high-frequency optical phonons (radial and tangential Au-S vibrations), and HOMO-to-LUMO transitions in $Au_{25}(SPh)_{18}^-$ and $Au_{25}(3.5-DMBT)_{18}^-$ mainly couple with low-frequency phonons. In other words, aromatic ligands change the energy relaxation pathway of HOMO-to-LUMO transitions in Au₂₅ NCs. The suppression of high-frequency optical phonons can be ascribed to two aspects. First, π electrons from the benzene rings of the aromatic ligands can conjugate with S atoms through a $p-\pi$ interaction that increases the electron density on S atoms and even the entire staple motif. The two methyl groups in the 3,5-DMBT ligand are electron donors and can result in a stronger effect. The Coulomb repulsion can lead to a stronger quantum confinement effect in aromaticligand-protected Au₂₅ NCs and suppress the core-shell charge transfer. Hence, the interaction between the staple phonon and the electronic transition is suppressed. The second factor is the steric effect of ligands. The aromatic ligands are much bulkier (sp² vs sp³ carbon) than nonaromatic ligands and provide more hindrance for vibrations, and the shorter distance between adjacent ligands can lead to a much stronger π - π stacking interaction. 30,59,60 In the Raman spectra and DFT simulations of Au₂₅ NCs, Au-S-C bending is the only vibrational mode that has frequencies between 170 and 200 cm⁻¹.^{26,49,61,62} Nevertheless, the nature of such a vibration makes it not possible to form strong electron-phonon interactions. Previous research on the Bose-Einstein two-oscillator model has noted that it is possible for the model to integrate high frequency acoustic phonons with the optical oscillator.³⁵ Here, we believe that the modeled high-frequency oscillator represents an average of the

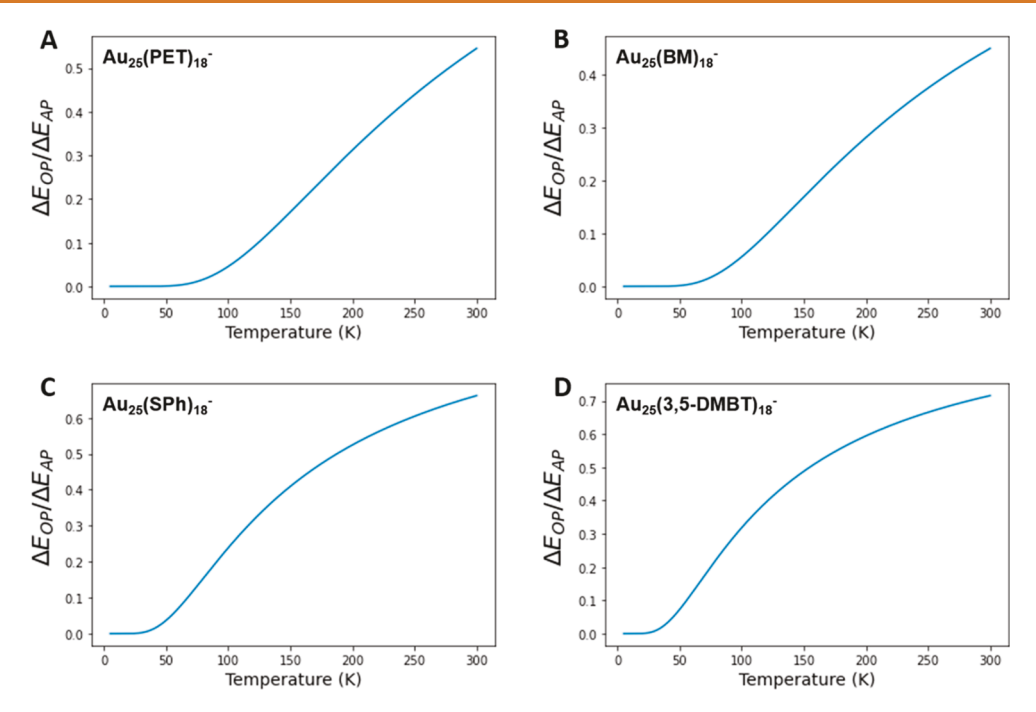


Figure 4. Ratio of contributions from optical phonon and acoustic phonon at different temperatures ($\Delta E_{\rm OP}/\Delta E_{\rm AP}$, $\Delta E_{\rm OP} = \alpha W_1(\hbar \omega_{\rm OP}/\exp(\hbar \omega_{\rm OP}/k_{\rm B}T)-1)$, $\Delta E_{\rm AP} = \alpha W_2(\hbar \omega_{\rm AP}/\exp(\hbar \omega_{\rm AP}/k_{\rm B}T)-1)$).

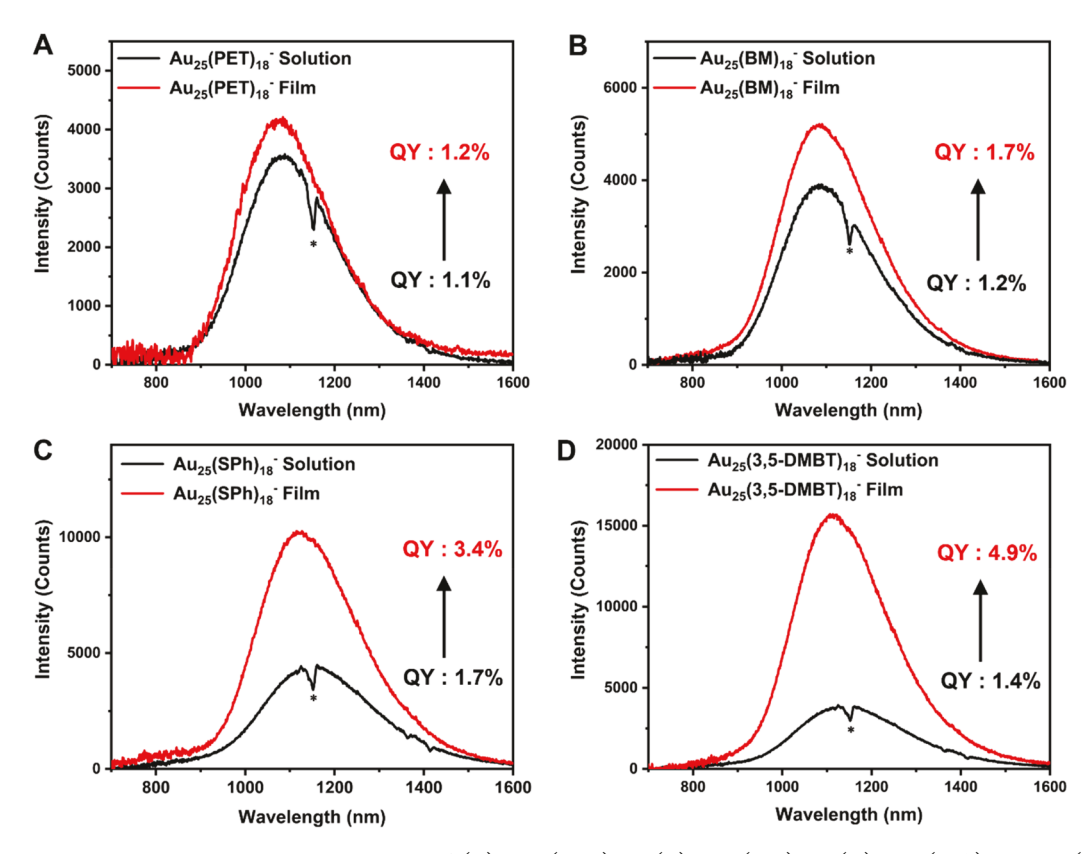


Figure 5. Room-temperature photoluminescence spectra of (A) $Au_{25}(PET)_{18}^-$, (B) $Au_{25}(BM)_{18}^-$, (C) $Au_{25}(SPh)_{18}^-$, and (D) $Au_{25}(3,5-DMBT)_{18}^-$ in solution (black line) and film (red line). Excitation: 375 nm. The asterisk indicates the reabsorption by DCM.

core breathing mode and Au–S vibrations in the motifs. Of note, such an integration is also possible in the case of $\mathrm{Au}_{25}(\mathrm{PET})_{18}^-$ and $\mathrm{Au}_{25}(\mathrm{BM})_{18}^-$ but the contribution from optical phonons is dominant.

To understand the relative contribution by acoustic phonons and optical phonons, we plot the $\Delta E_{\mathrm{OP}}/\Delta E_{\mathrm{AP}}$ from rt down to 4 K in Figure 4. It can be seen that the contribution from electron—acoustic-phonon interactions is stronger than that of electron—optical-phonon interactions in the entire temperature

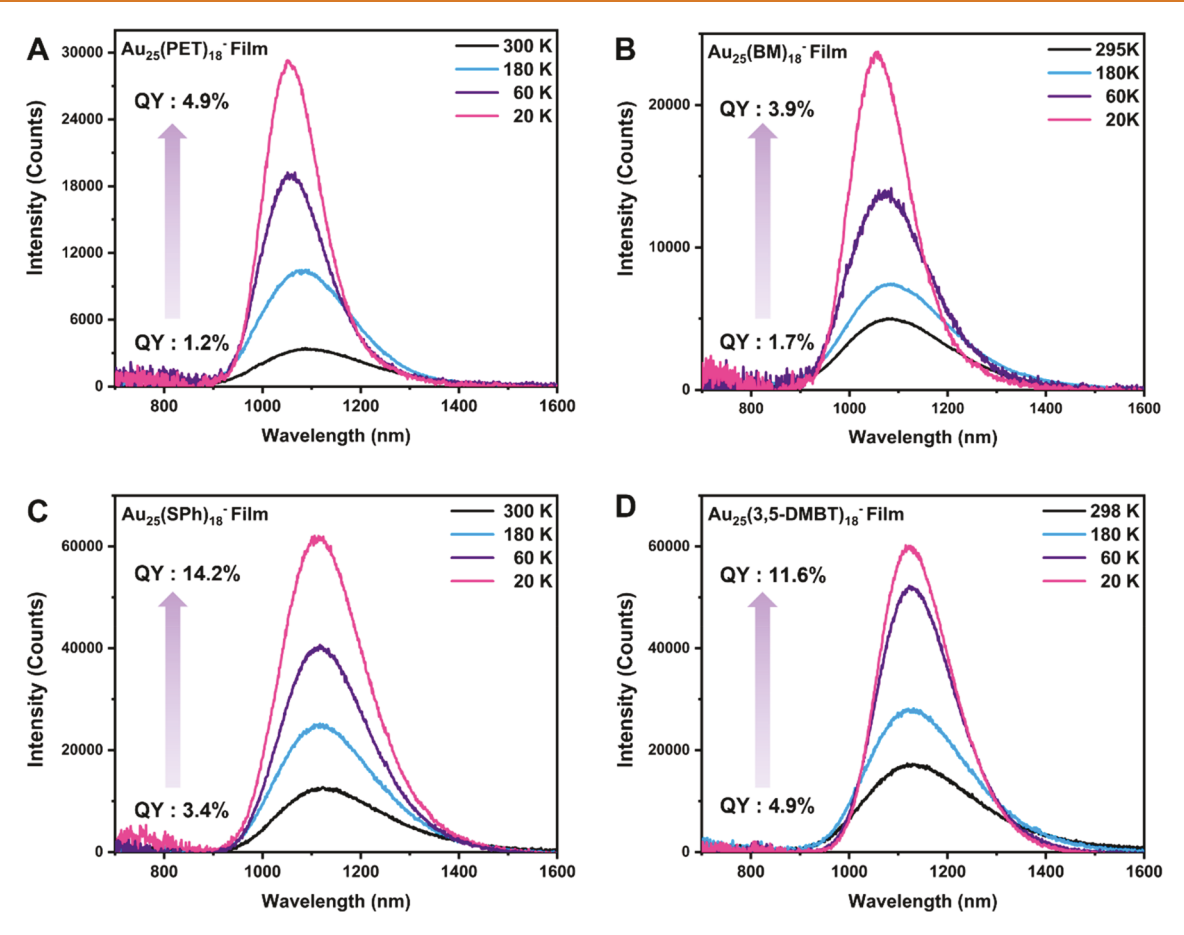


Figure 6. Cryogenic photoluminescence spectra of (A) $\text{Au}_{25}(\text{PET})_{18}^{-}$, (B) $\text{Au}_{25}(\text{BM})_{18}^{-}$, (C) $\text{Au}_{25}(\text{SPh})_{18}^{-}$, and (D) $\text{Au}_{25}(3,5\text{-DMBT})_{18}^{-}$ from room temperature down to 20 K. Excitation wavelength: 375 nm.

range. Especially, when the temperature goes down to 50-100 K, the contribution from optical phonons is trivial. If we consider the contribution of acoustic phonons to the modeled optical oscillator, the contribution from optical oscillator can be less. Therefore, our early assumption that both types of phonon modes should be considered is correct. The dominant effect of acoustic phonons is also consistent with the electronic HOMO-to-LUMO transition, which almost solely consists of wave functions of the Au_{13} core according to DFT simulations by Aikens and Jiang et al. 27,31

PL OF Au₂₅(SR)₁₈-NCs

The PL properties of $Au_{25}(SR)_{18}$ NCs and the origin of PL have long been an intriguing question ever since the structure was determined. 13 To shed light on it, tremendous experimental and theoretical efforts have been made in the past decade. 63-65 With years of work, it has been widely accepted that the PL emission of Au₂₅(SR)₁₈ NCs falls between 700 and 1600 nm. However, due to the limitations of common commercial visible and NIR detectors (<850 nm and >950 nm, respectively), a full picture of $Au_{25}(SR)_{18}^{-}$ NCs has not been obtained. Meanwhile, it is worth noting that, in air, $\mathrm{Au_{25}(SR)_{18}}^-$ NCs can easily be photo-oxidized to neutral $\left[\mathrm{Au_{25}(SR)_{18}}\right]^0$ (its PL peak centered at 800 nm) during PL measurements, which thus results in a distorted spectrum. Here, with a broadband detector (500-1700 nm), we measured the complete PL emission spectra of Au₂₅(SR)₁₈ NCs. To avoid the possible effects of oxidation and decomposition of Au₂₅(SR)₁₈ NCs, here we use freshly made samples and all the measurements are conducted under N₂ gas

or He gas. As shown in Figure 5A-D (black profiles), all four Au₂₅ NCs show a single emission peak that is centered around 1100 nm, with a 0.4 eV Stokes shift compared to their HOMO— LUMO absorption peak. Of note, the sharp drop at 1150 nm is due to reabsorption by dichloromethane (DCM; see Figure S3). The quantum yields (QYs) of the four samples were measured by a relative method with IR-1061 in DCM as a standard.⁶⁶ As shown in Figure 5, the four Au₂₅ NCs showed QYs of 1.1 to 1.7% in the DCM solution, indicating a ligand effect in the solution state. When we embedded Au₂₅ NCs into polystyrene films, the QYs of PET- and BM-protected Au₂₅ NCs increase by ~10% and 40% compared to their solutions, whereas the QYs of SPhand 3,5-DMBT-protected Au₂₅ NCs increased by several times. Such a distinct difference can be ascribed to the strong suppression of optical phonon branches in the aromaticligand-protected Au₂₅ NCs, as we illustrated in the above electron-phonon coupling analysis. We also used a visible photomultiplier tube (PMT-900) detector to measure the visible-region PL spectra (Figure S4A-D). Of note, the sharp drop starting at 850 nm in the PL spectra measured by PMT-900 is caused by the detector's limitation, whereas the broadband PMT-1700 detector extends from 500 to 1700 nm. The spectra between 600 and 900 nm that are measured by the two detectors are consistent.

The low QY indicates a significant loss of photoexcitation energy by nonradiative processes. To further understand the nonradiative relaxation process in Au_{25} NCs, cryogenic PL measurements for the four samples were carried out from room temperature down to 20 K. Similarly to the temperature-

dependent optical absorption spectra, the emission peak also showed a blue shift as the temperature decreased but was less significant (Figure 6A-D and Table S1). Previous research found that the QYs of Au23(SR)16 and [Au₂₁(SR)₁₂(PPh₂CH₂PPh₂)]⁺ reached over 70% when the temperature was decreased to 80 K. 12 Theoretically, if phononassisted nonradiative relaxation were the only nonradiative relaxation channel, the QY should reach near 100% when the temperature decreases to 4 K, because the phonon population will fall to near zero at 4 K. However, in the cases studied here, we found that the QY of all four Au₂₅ NCs did not approach 100% (QY < 20%) as the temperature was decreased to 20 K. At 20 K, the thermal energy is less than 2 meV, which can barely activate acoustic phonons and optical phonons. The observed temperature-dependent PL behavior indicates that the previously proposed luminescence mechanism for Au₂₅ NCs is not yet complete, and very low frequency acoustic phonons or nonphonon-assisted relaxations should be taken into consideration in future work.⁶⁴

CONCLUSION

In summary, we have presented an experimental and theoretical investigation of the vibrational relaxation in Au₂₅ NCs. Temperature-dependent optical absorption spectra of four Au₂₅ NCs protected by different ligands are measured from rt down to LH temperature. A Bose-Einstein two-oscillator model is introduced to describe the temperature-induced E_{g} renormalization. This work elucidates the detailed electron-phonon interaction mechanisms in Au₂₅ NCs. Acoustic phonons are identified as the main contributors to the E_g renormalization and nonradiative energy relaxation. Meanwhile, a suppression of high-frequency optical phonons is found in aromatic-ligandprotected Au₂₅ NCs and a PL spectroscopic analysis proved that such a suppression leads to PL enhancement. Overall, our current work on the electron-phonon interactions in Au₂₅ NCs provides guidances for an understanding of the mechanisms of PL and will promote the discovery of Au NCs with enhanced PL properties in future work.

METHODS

Synthesis of Au₂₅(SR)₁₈ $^-$ NCs. The synthesis of Au₂₅(PET)₁₈ $^-$ and Au₂₅(BM)₁₈ $^-$ followed a previously reported one-pot method. The synthesis of Au₂₅(SPh)₁₈ and Au₂₅(3,5-DMBT)₁₈ was achieved by a previously reported ligand-induced structure transformation method. Per a constant of the synthesis of Au₂₅(SPh)₁₈ and Au₂₅(3,5-DMBT)₁₈ was achieved by a previously reported ligand-induced structure transformation method.

Preparation of Au Nanoclusters/Polystyrene Composite Thin Film. A solid thin film was obtained by a drop-cast method. First of all, a polystyrene stock solution was prepared by dissolving polystyrene (80 mg) in 1 mL of $\mathrm{CH_2Cl_2}$. Meanwhile, the stock solution of $\mathrm{Au_{25}}$ NCs was prepared by dissolving 1 mg of $\mathrm{Au_{25}}$ NCs in 1 mL of $\mathrm{CH_2Cl_2}$. Then, 20 μ L of the as-obtained Au nanocluster solution and 10 μ L of polystyrene solution were mixed together to give an inklike solution. Finally, the solution was dropped on a quartz plate and dried slowly at room temperature.

Steady-State UV-Vis-NIR and Cryogenic Measurements. UV-vis-NIR spectra of Au nanoclusters were collected with a UV-3600 Plus UV-vis-NIR spectrophotometer (Shimadzu). The homebuilt low-temperature system included the UV-3600 Plus spectrometer, a vacuum pump, an Optistat CF2 cryostat (Oxford Instruments), and a temperature controller. Liquid helium was used as the cryogen.

Steady-State Photoluminescence and Cryogenic Measurements. Steady-state photoluminescence spectra were measured on a FLS-1000 spectrofluorometer (Edinburgh). Visible PL was measured using a photomultiplier (PMT) as the detector. Near-infrared PL was measured using a wide-range InGaAs detector cooled with liquid nitrogen (-80 °C). The home-built low-temperature system included

the FLS-1000 spectrofluorometer, a vacuum pump, an Optistat CF2 cryostat (Oxford Instruments), and a temperature controller. Liquid helium was used as the cryogen.

ASSOCIATED CONTENT

Supporting Information

The Supporting Information is available free of charge at https://pubs.acs.org/doi/10.1021/acsnano.2c06586.

Additional experimental details, including additional images of the absorption coefficients of four Au_{25} NCs at different wavelengths, an image of the quadrupolar mode of Au_{25} NCs, a transmission spectrum of dichloromethane, and visible region PL spectra of four Au_{25} NCs, and photoluminescence data of the four Au_{25} NCs at room temperature and 20 K (PDF)

AUTHOR INFORMATION

Corresponding Author

Rongchao Jin — Department of Chemistry, Carnegie Mellon University, Pittsburgh, Pennsylvania 15213, United States; orcid.org/0000-0002-2525-8345; Email: rongchao@andrew.cmu.edu

Authors

Zhongyu Liu — Department of Chemistry, Carnegie Mellon University, Pittsburgh, Pennsylvania 15213, United States; orcid.org/0000-0002-2777-8360

Yingwei Li — Department of Chemistry, Carnegie Mellon University, Pittsburgh, Pennsylvania 15213, United States; orcid.org/0000-0002-4813-6009

Ellen Kahng — Department of Chemistry, Carnegie Mellon University, Pittsburgh, Pennsylvania 15213, United States Shan Xue — Department of Chemistry, Carnegie Mellon University, Pittsburgh, Pennsylvania 15213, United States

Xiangsha Du — Department of Chemistry, Carnegie Mellon University, Pittsburgh, Pennsylvania 15213, United States; orcid.org/0000-0002-6508-866X

Site Li – Department of Chemistry, Carnegie Mellon University, Pittsburgh, Pennsylvania 15213, United States

Complete contact information is available at: https://pubs.acs.org/10.1021/acsnano.2c06586

Notes

The authors declare no competing financial interest.

ACKNOWLEDGMENTS

R.J. acknowledges the financial support from the NSF (DMR 1808675).

REFERENCES

- (1) Jin, R.; Zeng, C.; Zhou, M.; Chen, Y. Atomically Precise Colloidal Metal Nanoclusters and Nanoparticles: Fundamentals and Opportunities. *Chem. Rev.* **2016**, *116*, 10346–10413.
- (2) Du, Y.; Sheng, H.; Astruc, D.; Zhu, M. Atomically Precise Noble Metal Nanoclusters as Efficient Catalysts: A Bridge between Structure and Properties. *Chem. Rev.* **2020**, *120*, 526–622.
- (3) Jin, R.; Li, G.; Sharma, S.; Li, Y.; Du, X. Toward Active-Site Tailoring in Heterogeneous Catalysis by Atomically Precise Metal Nanoclusters with Crystallographic Structures. *Chem. Rev.* **2021**, *121*, 567–648.
- (4) Abbas, M. A.; Kamat, P. V.; Bang, J. H. Thiolated Gold Nanoclusters for Light Energy Conversion. *ACS Energy Lett.* **2018**, 3, 840–854.

- (5) Zhang, L.; Wang, E. Metal Nanoclusters: New Fluorescent Probes for Sensors and Bioimaging. *Nano Today* **2014**, *9*, 132–157.
- (6) Bain, D.; Maity, S.; Patra, A. Opportunities and Challenges in Energy and Electron Transfer of Nanocluster Based Hybrid Materials and Their Sensing Applications. *Phys. Chem. Chem. Phys.* **2019**, *21*, 5863–5881.
- (7) Matus, M. F.; Häkkinen, H. Atomically Precise Gold Nanoclusters: Towards an Optimal Biocompatible System from a Theoretical—Experimental Strategy. *Small* **2021**, *17*, 2005499.
- (8) Zuber, G.; Weiss, E.; Chiper, M. Biocompatible Gold Nanoclusters: Synthetic Strategies and Biomedical Prospects. *Nanotechnology* **2019**, *30*, 352001.
- (9) Mitsui, M.; Wada, Y.; Kishii, R.; Arima, D.; Niihori, Y. Evidence for Triplet-State-Dominated Luminescence in Biicosahedral Superatomic Molecular Au₂₅ Clusters. *Nanoscale* **2022**, *14*, 7974.
- (10) Andolina, C. M.; Crawford, S. E.; Smith, A. M.; Johnston, K. A.; Straney, P. J.; Marbella, L. E.; Tolman, N. L.; Hochuli, T. J.; Millstone, J. E. Near-Infrared Photoluminescence from Small Copper, Silver, and Gold Nanoparticles. *ChemNanoMat* **2018**, *4*, 265–268.
- (11) Li, Q.; Zeman, C. J., IV; Ma, Z.; Schatz, G. C.; Gu, X. W. Bright NIR-II Photoluminescence in Rod-Shaped Icosahedral Gold Nanoclusters. *Small* **2021**, *17*, 2007992.
- (12) Li, Q.; Zhou, M.; So, W. Y.; Huang, J.; Li, M.; Kauffman, D. R.; Cotlet, M.; Higaki, T.; Peteanu, L. A.; Shao, Z.; et al. A Mono-Cuboctahedral Series of Gold Nanoclusters: Photoluminescence Origin, Large Enhancement, Wide Tunability, and Structure—Property Correlation. J. Am. Chem. Soc. 2019, 141, 5314—5325.
- (13) Wu, Z.; Jin, R. On the Ligand's Role in the Fluorescence of Gold Nanoclusters. *Nano Lett.* **2010**, *10*, 2568–2573.
- (14) Gan, Z.; Lin, Y.; Luo, L.; Han, G.; Liu, W.; Liu, Z.; Yao, C.; Weng, L.; Liao, L.; Chen, J.; et al. Fluorescent Gold Nanoclusters with Interlocked Staples and a Fully Thiolate-Bound Kernel. *Angew. Chem., Int. Ed.* **2016**, *55*, 11567–11571.
- (15) Wu, Z.; Yao, Q.; Zang, S.-q.; Xie, J. Aggregation-Induced Emission in Luminescent Metal Nanoclusters. *Natl. Sci. Rev.* **2021**, 8, nwaa208.
- (16) Quan, L. N.; Park, Y.; Guo, P.; Gao, M.; Jin, J.; Huang, J.; Copper, J. K.; Schwartzberg, A.; Schaller, R.; Limmer, D. T.; et al. Vibrational Relaxation Dynamics in Layered Perovskite Quantum Wells. *Proc. Natl. Acad. Sci. U. S. A.* **2021**, *118*, No. e2104425118.
- (17) Devadas, M. S.; Bairu, S.; Qian, H.; Sinn, E.; Jin, R.; Ramakrishna, G. Temperature-Dependent Optical Absorption Properties of Monolayer-Protected Au₂₅ and Au₃₈ Clusters. *J. Phys. Chem. Lett.* **2011**, *2*, 2752–2758.
- (18) Liu, Z.; Li, Y.; Shin, W.; Jin, R. Observation of Core Phonon in Electron–Phonon Coupling in Au_{25} Nanoclusters. *J. Phys. Chem. Lett.* **2021**, *12*, 1690–1695.
- (19) Yu, S.; Xu, J.; Shang, X.; Ma, E.; Lin, F.; Zheng, W.; Tu, D.; Li, R.; Chen, X. Unusual Temperature Dependence of Bandgap in 2D Inorganic Lead-Halide Perovskite Nanoplatelets. *Adv. Sci.* **2021**, *8*, 2100084
- (20) Gong, X.; Voznyy, O.; Jain, A.; Liu, W.; Sabatini, R.; Piontkowski, Z.; Walters, G.; Bappi, G.; Nokhrin, S.; Bushuyev, O.; et al. Electron—Phonon Interaction in Efficient Perovskite Blue Emitters. *Nat. Mater.* **2018**, *17*, 550–556.
- (21) O'donnell, K.; Chen, X. Temperature Dependence of Semiconductor Band Gaps. *Appl. Phys. Lett.* **1991**, *58*, 2924–2926.
- (22) Bhosale, J.; Ramdas, A.; Burger, A.; Muñoz, A.; Romero, A.; Cardona, M.; Lauck, R.; Kremer, R. Temperature Dependence of Band Gaps in Semiconductors: Electron-Phonon Interaction. *Phys. Rev. B* **2012**, *86*, 195208.
- (23) Peng, B.; Li, J.; Li, Q.; Li, Y.; Zhu, H.; Zhang, L.; Wang, X.; Bi, L.; Lu, H.; Xie, J.; et al. Bose–Einstein Oscillators and the Excitation Mechanism of Free Excitons in 2D Layered Organic–Inorganic Perovskites. *RSC Adv.* **2017**, *7*, 18366–18373.
- (24) Devadas, M. S.; Thanthirige, V. D.; Bairu, S.; Sinn, E.; Ramakrishna, G. Temperature-Dependent Absorption and Ultrafast Luminescence Dynamics of Bi-icosahedral Au₂₅ Clusters. *J. Phys. Chem.* C 2013, 117, 23155–23161.

- (25) Maioli, P.; Stoll, T.; Sauceda, H. E.; Valencia, I.; Demessence, A.; Bertorelle, F.; Crut, A.; Vallee, F.; Garzon, I. L.; Cerullo, G.; et al. Mechanical Vibrations of Atomically Defined Metal Clusters: From Nano-to Molecular-Size Oscillators. *Nano Lett.* **2018**, *18*, 6842–6849.
- (26) Krishnadas, K. R.; Baghdasaryan, A.; Kazan, R.; Banach, E.; Teyssier, J.; Nicu, V. P.; Buergi, T. Raman Spectroscopic Fingerprints of Atomically Precise Ligand Protected Noble Metal Clusters: Au₃₈(PET)₂₄ and Au_{38-x}Ag_x(PET)₂₄. Small **2021**, 17, 2101855.
- (27) Zhu, M.; Aikens, C. M.; Hollander, F. J.; Schatz, G. C.; Jin, R. Correlating the Crystal Structure of a Thiol-Protected Au₂₅ Cluster and Otical Poperties. *J. Am. Chem. Soc.* **2008**, *130*, 5883–5885.
- (28) Wu, Z.; Suhan, J.; Jin, R. One-Pot Synthesis of Atomically Monodisperse, Thiol-Functionalized Au₂₅ Nanoclusters. *J. Mater. Chem.* **2009**, *19*, 622–626.
- (29) Maman, M. P.; Nair, A. S.; Abdul Hakkim Nazeeja, A. M.; Pathak, B.; Mandal, S. Synergistic Effect of Bridging Thiolate and Hub Atoms for the Aromaticity Driven Symmetry Breaking in Atomically Precise Gold Nanocluster. *J. Phys. Chem. Lett.* **2020**, *11*, 10052–10059.
- (30) Li, G.; Abroshan, H.; Liu, C.; Zhuo, S.; Li, Z.; Xie, Y.; Kim, H. J.; Rosi, N. L.; Jin, R. Tailoring the Electronic and Catalytic Properties of Au₂₅ Nanoclusters via Ligand Engineering. *ACS Nano* **2016**, *10*, 7998–8005.
- (31) Jiang, D.-e.; Kühn, M.; Tang, Q.; Weigend, F. Superatomic Orbitals under Spin-Orbit Coupling. *J. Phys. Chem. Lett.* **2014**, *5*, 3286–3289
- (32) Du, X.; Liu, Z.; Higaki, T.; Zhou, M.; Jin, R. Understanding the Nascent Plasmons and Metallic Bonding in Atomically Precise Gold Nanoclusters. *Chem. Sci.* **2022**, *13*, 1925–1932.
- (33) Galchenko, M.; Black, A.; Heymann, L.; Klinke, C. Field Effect and Photoconduction in Au₂₅ Nanoclusters Films. *Adv. Mater.* **2019**, 31, 1900684.
- (34) Wang, S.; Ma, J.; Li, W.; Wang, J.; Wang, H.; Shen, H.; Li, J.; Wang, J.; Luo, H.; Li, D. Temperature-Dependent Band Gap in Two-Dimensional Perovskites: Thermal Expansion Interaction and Electron—Phonon Interaction. *J. Phys. Chem. Lett.* **2019**, *10*, 2546—2553.
- (35) Pässler, R. Temperature Dependence of Fundamental Band Gaps in Group IV, III—V, and II—VI Materials via a Two-Oscillator Model. *J. Appl. Phys.* **2001**, *89*, 6235–6240.
- (36) Pässler, R. Moderate Phonon Dispersion Shown by the Temperature Dependence of Fundamental Band Gaps of Various Elemental and Binary Semiconductors Including Wide-Band Gap Materials. J. Appl. Phys. 2000, 88, 2570–2577.
- (37) Pässler, R. Dispersion-Related Description of Temperature Dependencies of Band Gaps in Semiconductors. *Phys. Rev. B* **2002**, *66*, No. 085201.
- (38) Morris, D. J.; Yang, R.; Higaki, T.; Ward, M. J.; Jin, R.; Zhang, P. Core Geometry Effect on the Bonding Properties of Gold—Thiolate Nanoclusters: The Case of Hexagonal-Close-Packed Au₃₀(SR)₁₈. *J. Phys. Chem. C* **2018**, *122*, 23414–23419.
- (39) Chen, Y.; Gao, Q.; Wang, Y.; An, X.; Liao, X.; Mai, Y.-W.; Tan, H. H.; Zou, J.; Ringer, S. P.; Jagadish, C. Determination of Young's Modulus of Ultrathin Nanomaterials. *Nano Lett.* **2015**, *15*, 5279–5283.
- (40) Li, Q.; Zhou, D.; Chai, J.; So, W. Y.; Cai, T.; Li, M.; Peteanu, L. A.; Chen, O.; Cotlet, M.; Wendy Gu, X.; Zhu, H.; Jin, R. Structural Distortion and Electron Redistribution in Dual-Emitting Gold Nanoclusters. *Nat. Commun.* **2020**, *11*, 2897.
- (41) Li, Q.; Mosquera, M. A.; Jones, L. O.; Parakh, A.; Chai, J.; Jin, R.; Schatz, G. C.; Gu, X. W. Pressure-Induced Optical Transitions in Metal Nanoclusters. *ACS Nano* **2020**, *14*, 11888–11896.
- (42) Monserrat, B.; Drummond, N.; Needs, R. Anharmonic Vibrational Properties in Periodic Systems: Energy, Electron-Phonon Coupling, and Stress. *Phys. Rev. B* **2013**, *87*, 144302.
- (43) Tilchin, J.; Dirin, D. N.; Maikov, G. I.; Sashchiuk, A.; Kovalenko, M. V.; Lifshitz, E. Hydrogen-Like Wannier—Mott Excitons in Single Crystal of Methylammonium Lead Bromide Perovskite. *ACS Nano* **2016**, *10*, 6363–6371.
- (44) Snoke, D. W.Solid State Physics: Essential Concepts; Cambridge University Press: 2020.

- (45) Bürgi, T. Properties of the Gold-Sulphur Interface: from Self-Assembled Monolayers to Clusters. Nanoscale 2015, 7, 15553-15567.
- (46) Nieto-Ortega, B.; Bürgi, T. Vibrational Properties of Thiolate-Protected Gold Nanoclusters. Acc. Chem. Res. 2018, 51, 2811-2819.
- (47) Stroscio, M. A.; Kim, K.; Yu, S.; Ballato, A. Quantized Acoustic Phonon Modes in Quantum Wires and Quantum Dots. J. Appl. Phys. 1994, 76, 4670-4675.
- (48) Hartland, G. V. Optical Studies of Dynamics in Noble Metal Nanostructures. Chem. Rev. 2011, 111, 3858-3887.
- (49) Tlahuice-Flores, A.; Whetten, R. L.; Jose-Yacaman, M. Vibrational Normal Modes of Small Thiolate-Protected Gold Clusters. J. Phys. Chem. C 2013, 117, 12191-12198.
- (50) Varnholt, B.; Guberman-Pfeffer, M. J.; Oulevey, P.; Antonello, S.; Dainese, T.; Gascón, J. A.; Bürgi, T.; Maran, F. Vibrational Coupling Modulation in n-Alkanethiolate Protected $Au_{25}(SR)_{18}^{0}$ Clusters. *J. Phys.* Chem. C 2016, 120, 25378-25386.
- (51) Bardeen, J.; Shockley, W. Deformation Potentials and Mobilities in Non-Polar Crystals. Phys. Rev. 1950, 80, 72.
- (52) Wright, A. D.; Verdi, C.; Milot, R. L.; Eperon, G. E.; Pérez-Osorio, M. A.; Snaith, H. J.; Giustino, F.; Johnston, M. B.; Herz, L. M. Electron-Phonon Coupling in Hybrid Lead Halide Perovskites. Nat. Commun. 2016, 7, 11755.
- (53) Guo, Z.; Wu, X.; Zhu, T.; Zhu, X.; Huang, L. Electron-Phonon Scattering in Atomically Thin 2D Perovskites. ACS Nano 2016, 10, 9992-9998.
- (54) Kong, J.; Wu, Y.-z.; Zhou, M. Coherent Vibrational Dynamics of $[Au_{25}(SR)_{18}]^-$ Nanoclusters. Chin. J. Chem. Phys. **2021**, 34, 598–604.
- (55) Qian, H.; Sfeir, M. Y.; Jin, R. Ultrafast Relaxation Dynamics of [Au₂₅(SR)₁₈]^q Nanoclusters: Effects of Charge State. J. Phys. Chem. C 2010, 114, 19935-19940.
- (56) Sfeir, M. Y.; Qian, H.; Nobusada, K.; Jin, R. Ultrafast Relaxation Dynamics of Rod-Shaped 25-Atom Gold Nanoclusters. J. Phys. Chem. C 2011, 115, 6200-6207.
- (57) Crut, A.; Maioli, P.; Del Fatti, N.; Vallée, F. Anisotropy Effects on the Time-Resolved Spectroscopy of the Acoustic Vibrations of Nanoobjects. Phys. Chem. Chem. Phys. 2009, 11, 5882-5888.
- (58) Yokoyama, T.; Hirata, N.; Tsunoyama, H.; Eguchi, T.; Negishi, Y.; Nakajima, A. Vibrational Spectra of Thiolate-Protected Gold Nanocluster with Infrared Reflection Absorption Spectroscopy: Sizeand Temperature-Dependent Ordering Behavior of Organic Monolayer. J. Phys. Chem. C 2020, 124, 363-371.
- (59) Higaki, T.; Zeng, C.; Chen, Y.; Hussain, E.; Jin, R. Controlling the Crystalline Phases (FCC, HCP and BCC) of Thiolate-Protected Gold Nanoclusters by Ligand-Based Strategies. CrystEngComm 2016, 18, 6979-6986.
- (60) Wang, S.; Tang, L.; Cai, B.; Yin, Z.; Li, Y.; Xiong, L.; Kang, X.; Xuan, J.; Pei, Y.; Zhu, M. Ligand Modification of Au₂₅ Nanoclusters for Near-Infrared Photocatalytic Oxidative Functionalization. J. Am. Chem. Soc. 2022, 144, 3787-3792.
- (61) Parker, J. F.; Choi, J.-P.; Wang, W.; Murray, R. W. Electron Self-Exchange Dynamics of the Nanoparticle Couple $[{\rm Au_{25}(SC_2Ph)_{18}}]^{0/1-}$ by Nuclear Magnetic Resonance Line-Broadening. J. Phys. Chem. C 2008, 112, 13976-13981.
- (62) Varnholt, B.; Oulevey, P.; Luber, S.; Kumara, C.; Dass, A.; Bürgi, T. Structural Information on the Au-S Interface of Thiolate-Protected Gold Clusters: a Raman Spectroscopy Study. J. Phys. Chem. C 2014, 118, 9604-9611.
- (63) Zhou, M.; Song, Y. Origins of Visible and Near-Infrared Emissions in $[Au_{25}(SR)_{18}]^-$ Nanoclusters. J. Phys. Chem. Lett. **2021**, 12, 1514-1519.
- (64) Weerawardene, K. D. M.; Aikens, C. M. Theoretical Insights into the Origin of Photoluminescence of $Au_{25}(SR)_{18}$ Nanoparticles. J. Am. Chem. Soc. 2016, 138, 11202-11210.
- (65) Suyama, M.; Takano, S.; Tsukuda, T. Synergistic Effects of Pt and Cd Codoping to Icosahedral Au₁₃ Superatoms. J. Phys. Chem. C 2020, 124, 23923-23929.
- (66) Hoshi, R.; Suzuki, K.; Hasebe, N.; Yoshihara, T.; Tobita, S. Absolute Quantum Yield Measurements of Near-Infrared Emission

with Correction for Solvent Absorption. Anal. Chem. 2020, 92, 607-

□ Recommended by ACS

Water-Soluble Au₂₅ Clusters with Single-Crystal Structure for Mitochondria-Targeting Radioimmunotherapy

Yue Hua, Shuang-Quan Zang, et al.

APRIL 06, 2023 ACS NANO

READ **C**

Nonlinear Optical Studies of [Pt₁₇(CO)₁₂(PPh₃)₈] n+ Metal Nanoclusters and Their Enhancement via All-Plastic **Photonic Crystal Cavity**

Athulya Kadeprath Satheesan, Chandrasekharan Keloth, et al. DECEMBER 27, 2022

THE JOURNAL OF PHYSICAL CHEMISTRY C

READ **C**

Isomer-Selective Conversion of Au Clusters by Au(I) **Thiolate Insertion**

Yuki Chiga, Toshiharu Teranishi, et al.

JUNE 21, 2023

INORGANIC CHEMISTRY

RFAD 1

Synchronous Metal Rearrangement on Two-Dimensional Equatorial Surfaces of Au-Cu Alloy Nanoclusters

Li Tang, Shuxin Wang, et al.

MARCH 06, 2023

ACS NANO

READ **C**

Get More Suggestions >